COMPARISON OF 2-D PROFILES OF CIV VACUUM ULTRA VIOLET RADIATION FROM THE UPPER AND LOWER DIVERTORS OF DIII–D

N.W. JALUFKA,[1] M.E. FENSTERMACHER,[2] G.D. PORTER,[2] N.S. WOLF,[2] A.W. LEONARD,[3] T.W. PETRIE,[3] R. ELLIS,[2] AND W. MEYER[2]

[1]Hampton University, Hampton, Virginia 23668 USA
[2]Lawrence Livermore National Laboratory, Livermore, California 94551 USA
[3]General Atomics, San Diego, California 92186-5608 USA

Abstract — 2-D poloidal profiles of vacuum ultra violet CIV radiation (155 nm) were obtained for the lower, open divertor and the closed, upper divertor in DIII–D using data from tangentially viewing camera systems. For these high triangularity discharges the data show that for both attached and detached plasmas the emission from visible CIII (456 nm) occurs at nearly the same locations as that from VUV CIV. This is consistent with earlier observations in the lower divertor for low triangularity, lower single-null discharges. Emission profiles from CIV agree qualitatively with tomographic reconstructions from a 48-channel bolometer array for both the upper baffled and lower open divertors at high triangularity. Finally, comparisons of the CIV profiles from the open vs. closed divertors show some significant differences in both attached and detached divertor operation. These may be the result of either the changes in divertor baffling geometry or due to magnetic field dependent particle drifts. The measured profiles were also compared to profiles generated by the UEDGE fluid code for both attached and detached plasmas.

1. INTRODUCTION

Reduction of the heat load to the divertor plates is an area of intense plasma physics research in tokamaks. Materials that are currently available can not withstand the heat load that is anticipated in larger tokamaks such as ITER [1]. One concept that shows considerable promise in this area is the radiative divertor [2–4 and references therein]. In this concept the energy in the divertor plasma is reduced using upstream scrape-off-layer (SOL) radiation. In DIII–D, radiation from the CIV doublet at 155 nm accounts for over 50% of the radiation emitted from the divertor in some types of discharges [5]. This is especially true for partially detached divertor (PDD) operation where neutral gas injection reduces the particle flow to the target plates and significantly reduces the divertor temperature [6].

Carbon is a significant contributor to the physics of the divertor in any tokamak with carbon plasma facing components, and it is necessary to understand the role it plays, particularly in the divertor power balance. To evaluate carbon effects at DIII–D experimental studies focus on CII and CIII emission in the visible and CIV emission in the vacuum ultra violet (VUV). The experimental work concentrates on the use of data from tangentially viewing cameras [7,8] to generate 2-D profiles in a poloidal plane of the carbon emission in the divertor. In addition, a strong modeling effort is underway to understand the physical processes in the divertor. This effort concentrates on the use of the UEDGE fluid code [9] to calculate the distributions of the various components in the discharge.

This paper is organized as follows. Section 2 presents a description of the discharges from which CIV, CIII and total radiated power profiles are compared. Section 3 then presents the 2-D profiles of the carbon species and the results of the reconstructions of the bolometer data. Initial results from fluid plasma simulations are given in Section 4. A summary and some preliminary conclusions are presented in the final section.

2. DISCHARGE DESCRIPTION

Studies of the carbon radiation from the two different divertors in DIII–D will provide information on the spatial profile and temporal evolution of the radiating volume and the relative radiative efficiency of the two designs. A cross section of the DIII–D equilibrium plasma shape and vacuum chamber illustrating the differences between the two divertors is shown in Fig. 1. In comparison, the upper, closed divertor is narrower and deeper, and it has an outer baffle, an inner private flux region dome baffle and inner and outer cryopumps. The design of the upper, closed divertor was optimized for high triangularity plasmas. In both cases the high triangularity shape puts the inner strikepoint on the vertical centerpost tiles and the outer strikepoint on a horizontal tile. Studies of this equilibrium indicate that changes in shape or position during the discharge are negligible. Discharge 102458 is a lower single-null (LSN) discharge while discharge 107344 is an upper single-null (USN). Both discharges are high triangularity with gas injection to produce a PDD discharge. In both cases the ion ∇B drift direction was down toward the lower divertor region.

The upper single-null discharge was chosen from the limited data available with the new upper VUV CIV camera system and then a lower single-null plasma was identified with very similar discharge conditions before and after detachment. Figure 2 displays the time history

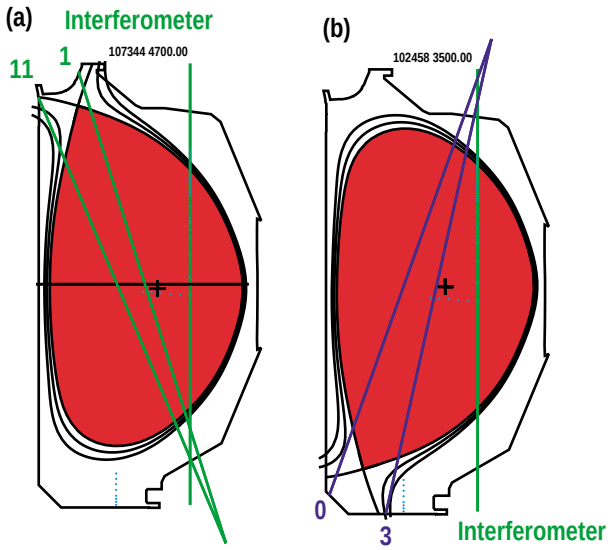

Fig. 1. Geometry of the upper single-null (USN) plasma (a) and the lower single-null (LSN) plasma (b) in the DIII–D vacuum vessel. SOL flux surfaces spacing at the midplane is 1 cm. Chords for line integral measurements of Dα emission (upper divertor channels 1, 11 and lower divertor channels 0, 3) and for line averaged density (interferometer) are shown.

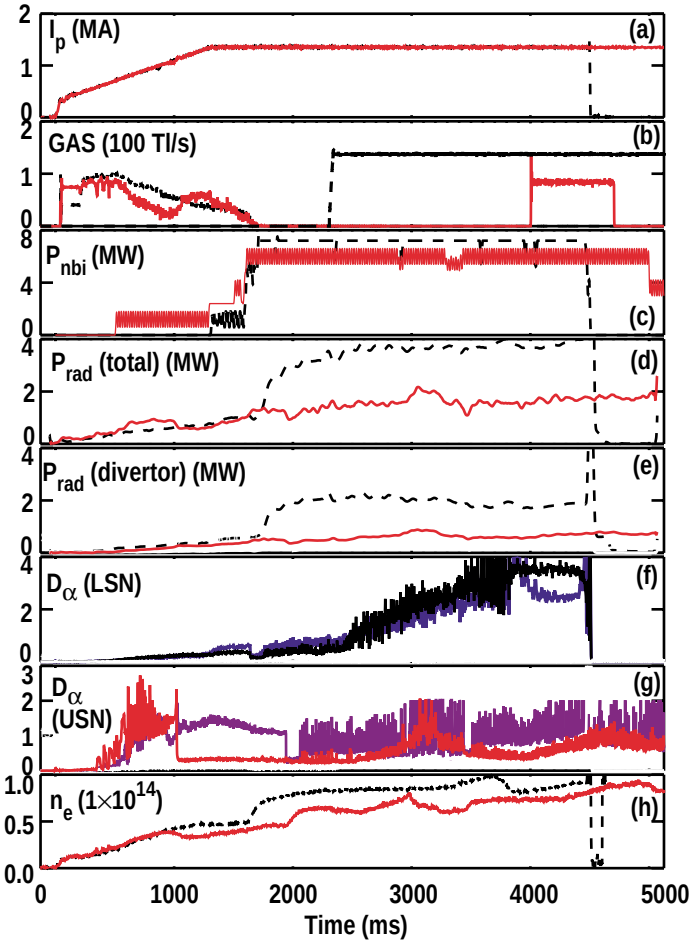

Fig. 2. Time evolution of discharge parameters for the USN closed divertor (red, solid, #107344) and LSN open divertor (black, dashed, #102458) plasmas used in this paper. Traces shown are (a), plasma current, (b) gas injection rate (c) neutral beam injected power, (d) total radiated power (e) radiated power from the divertor region, (f) $D\alpha$ emission from the lower divertor inner (blue) and outer (black) strikepoint regions, (g) $D\alpha$ emission from the upper divertor inner (purple) and outer (red) strikepoints, and (h) line averaged density.

of several parameters for the two discharges. Both were single-null discharges with gas injection so that both attached and detached plasmas could be studied. The ranges for other common discharge parameters for the two plasmas are: plasma current, I_p = 1.34 MA, toroidal field, B_T = 1.8–2.0 T, major radius, R_0 = 1.74 m, minor radius, a = 0.6 m, elongation, κ = 1.7, injected neutral beam power, P_{inj} = 6–6.7 MW, and safety factor at 95% flux, q_{95} = 3.7–4.0. However, matched USN and LSN discharges with VUV CIV image data and ion ∇B drift into the divertor in both cases were not available. Therefore, one significant difference between the discharges is that the B x $\nabla|B|$ drift for ions (hereafter referred to as the ion ∇B drift) is into the divertor for the LSN and away from the divertor for the USN. Another difference is the time of gas injection. In 102458 (LSN) the gas injection occurs at 2300 ms while in 107344 (USN) injection occurs later in the discharge at 4000 ms. In order to make as fair a comparison as possible between the two detached plasmas, the time of comparison was taken to be about 700 ms after the gas injection so that the two profiles were actually taken at the same stage of detachment. The densities before and after gas injection were similar.

3. EXPERIMENTAL RESULTS

Studies of CIII and CIV were carried out on the two discharges using tangentially viewing TVs. These devices are of a catadioptric design with an inverse Cassegrain form using a three mirror Wide Angle Large Reflective Unobscured System (WALRUS) configuration [8]. In both the visible and vacuum ultra violet systems, wavelength is selected by narrow band interference filters. Visible images are focussed directly onto a Charge Induction Device (CID) camera (~512 × 512 pixels) which records the images on standard video tape. For the vacuum ultra violet system a MgF_2 lens serves as a vacuum window between the main vacuum vessel of DIII–D and the optical system which is in a secondary vacuum chamber. This lens plus a 155 nm filter forms an ultra violet image of CIV radiation that is focussed onto a P1 phosphor within the secondary vacuum. The phosphor converts the VUV image to visible light (~550 nm) and this image is recorded by a CID camera outside the secondary vacuum. These 3-D images are digitized and reconstructions of 2-D profiles in a poloidal plane are generated using a matrix inversion process assuming toroidal symmetry [7].

Comparisons of the CIV VUV data, CIII visible emission, and reconstructions of total radiation data from bolometers (Figs. 3 and 4) from the new upper and lower divertors provides the opportunity to examine three topics: 1) the spatial profiles of VUV CIV radiation versus CIII visible emission in the same plasma, 2) the CIV spatial profile versus the total radiated power profile as reconstructed from the bolometer data in a highly baffled divertor and 3) the CIV, CIII and total radiation profiles from the well baffled (closed) upper divertor with ion ∇B drift away from the divertor versus the unbaffled (open) lower divertor with ion ∇B drift toward the divertor. Topic (1) is important because CIII visible emission is relatively easy to measure in tokamak divertors but the majority of the radiated power from carbon is lost from most divertor plasmas in the 155 nm CIV VUV line which is difficult to measure in 2-D or 3-D. Topic (2) represents a double check on the reconstructions of CIV emission from the camera data since it should correspond to the majority of the bolometer signal in many parts of the divertor. Finally topic (3) addresses the physics of changes in

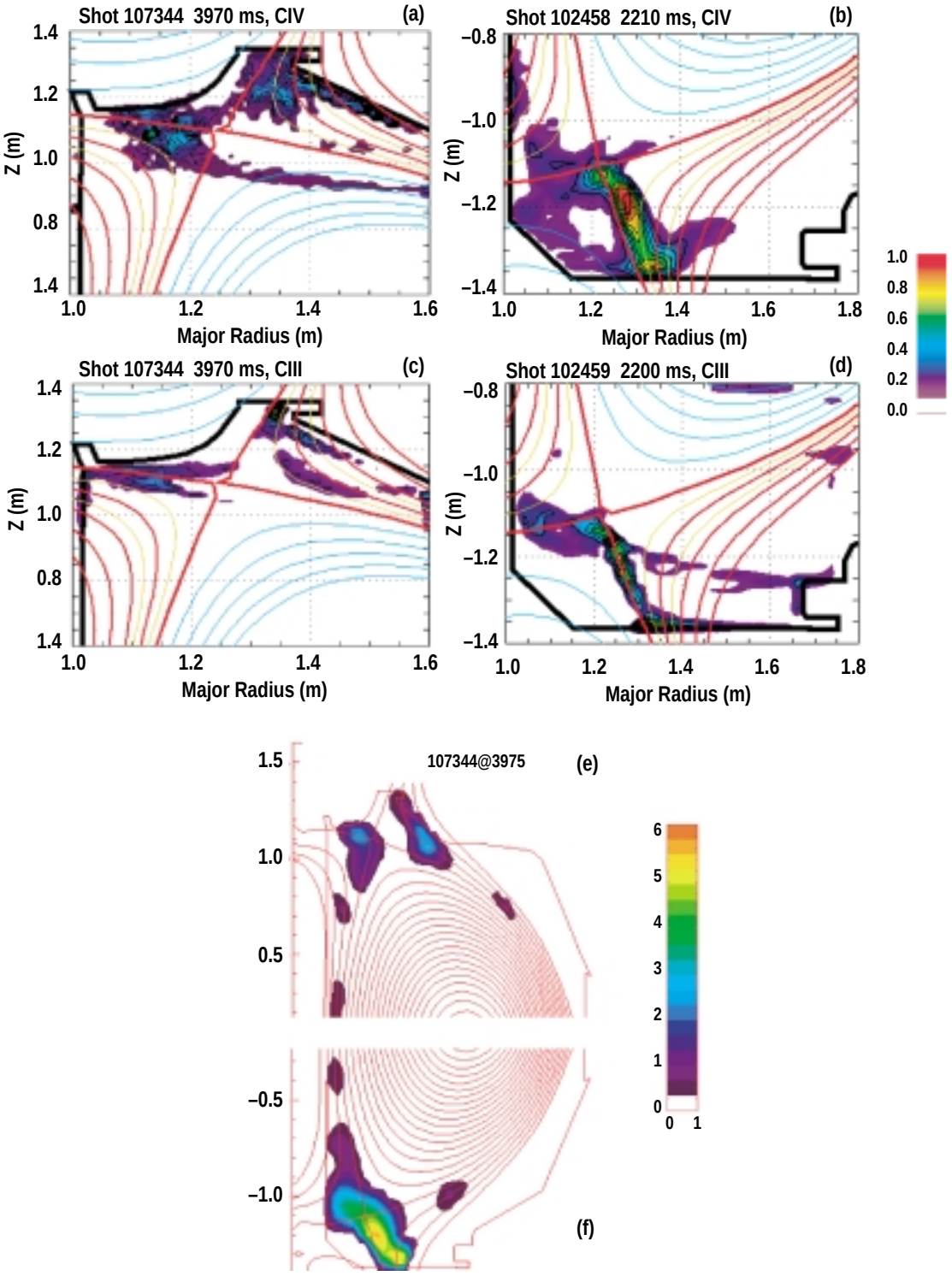

Fig. 3. 2-D profiles of CIV (a,b) and CIII (c,d) (arbitrary units), and reconstructions of total radiated power, P_{rad} (MW/m^3) (e,f) for the attached plasmas. Each carbon image is from a different camera. Relative intensity can not be compared between cameras but it can be compared for the same camera between attached and detached conditions (Fig. 4). Separatrix and SOL flux surfaces at 1cm intervals (mapped to the midplane) shown in red for (a–d); flux surfaces at 0.5 and 1.5 cm shown in yellow. SOL flux surfaces in (e),(f) at 2 cm intervals.

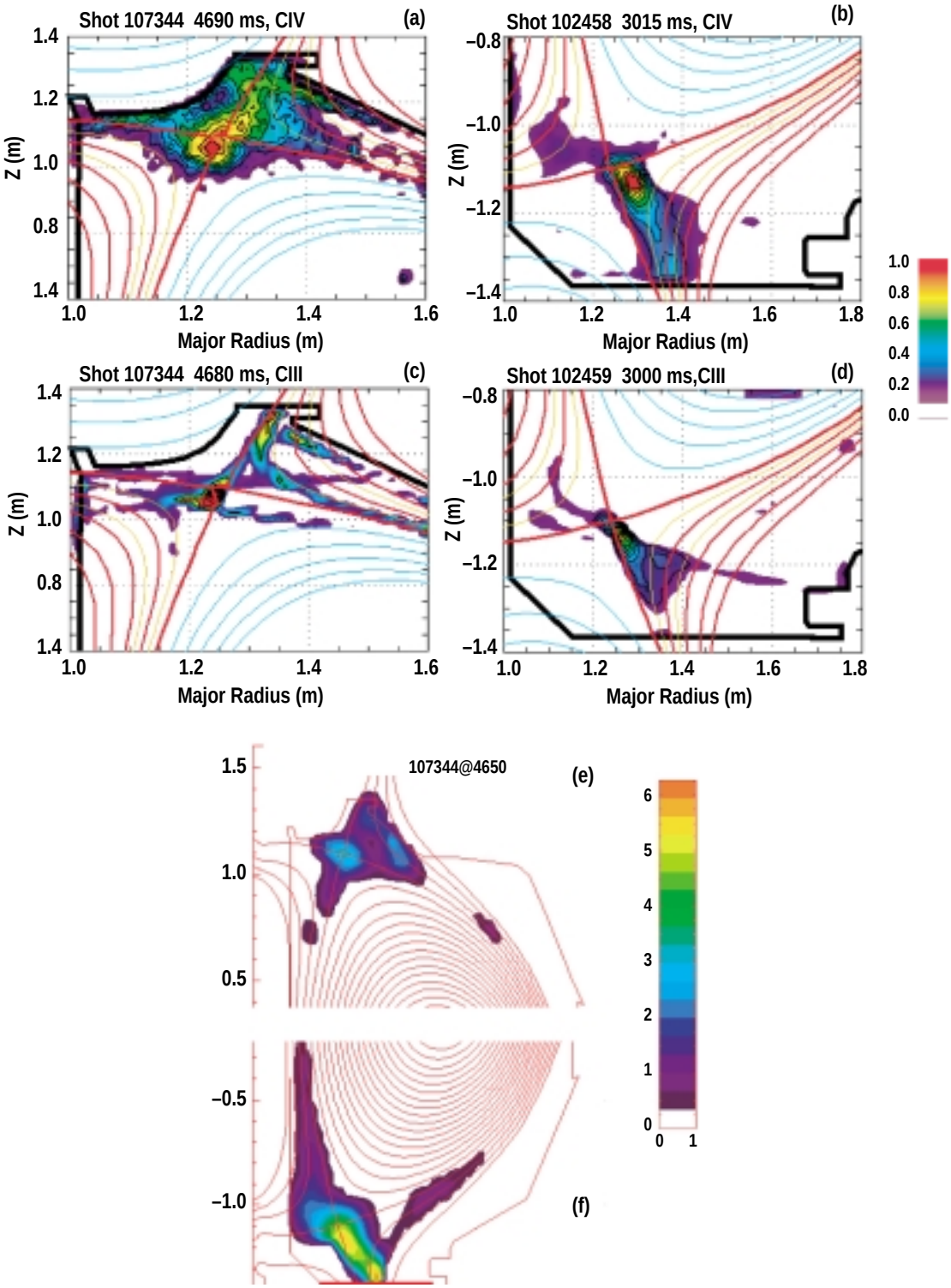

Fig. 4. 2-D profiles of CIV (a,b) and CIII (c,d) (arbitrary units), and reconstructions of total radiated power, P_{rad} (MW/m^3) (e,f) for the detached plasmas. Each carbon image is from a different camera. Relative intensity can not be compared between cameras but it can be compared for the same camera between attached and detached conditions (Fig. 3). Separatrix and SOL flux surfaces at 1cm intervals (mapped to the midplane) shown in red for (a–d); flux surfaces at 0.5 and 1.5 cm shown in yellow. SOL flux surfaces in (e),(f) at 2 cm intervals.

divertor operation both with ion ∇B drift direction and when baffling is installed. Each of these issues is addressed separately below.

Comparisons of CIII visible emission profiles with CIV VUV emission profiles in the new upper baffled divertor (Topic 1) shows that CIII measurements still give a good indication of the location of the main carbon radiation; this agrees with the conclusions from studies of low triangularity plasmas in the lower, open divertor [10]. The profiles of CIV VUV emission from the upper divertor in attached and detached ELMing H–mode operation are shown in Figs. 3(a) and 4(a) respectively. The corresponding profiles of CIII visible emission from the same discharge are shown in Figs. 3(c) and 4(c) respectively. In the attached case (Fig. 3) both the CIV and CIII profiles show that the emission comes from inner leg SOL near the X–point and from the outer leg near the target plate and outer baffle. In both of these emission regions the CIII emission is farther down the divertor leg than the CIV emission. This is consistent with previous measurements in the lower divertor, low triangularity attached plasmas and with collisional radiative modeling that indicates that the CIII emission comes from divertor plasma at slightly lower temperature than that which radiates in CIV [5]. For attached plasmas one would expect the lower temperature plasma to be farther down the divertor leg. The results for detached outer leg operation show CIV emission throughout the outer divertor leg with a local maxima near the X–point and strikepoint regions while the CIII emission profiles are more locally peaked at both the strikepoint and near the X–point. Detailed modeling will be required to determine if the temperature gradients around the X–point are sufficient to explain whether these measurements are completely consistent.

Comparisons of 2-D radiated power profiles from reconstructions of bolometer measurements and CIV VUV emission in the upper baffled divertor (Topic 2) show good correlation of the spatial profiles supporting previous conclusions from the lower open divertor that CIV is a main contributor to the total radiated power. The 2-D reconstructions of total radiated power from the bolometers in the upper divertor are shown in Figs. 3(e) and 4(e) for the attached and detached conditions respectively, corresponding to the CIV profiles in Figs. 3(a) and 4(a). Comparing the CIV and bolometer profiles shows that most of the features of the CIV profiles are reproduced in the bolometer reconstructions except radiation near the outer strikepoint. The bolometer arrays have good spatial coverage of the upper divertor with crossed view chords except for the region deep in the slot of the outer divertor. The lack of crossed views explains why the bolometer reconstructions do not show as much radiation in the vicinity of the outer strikepoint as the CIV images. The emission in the inner divertor leg during attached operation and the local maximum at the X–point in the detached case show good agreement between bolometer measurements and CIV images.

Comparisons of CIV emission in high triangularity baffled divertor plasma with ion ∇B drift out of the divertor and high triangularity open divertor plasmas with ion ∇B drift into the divertor (Topic 3) shows significant differences in the profiles both in attached ELMing H–mode before deuterium gas injection and in detached H–mode after gas injection. Comparisons of open versus closed CIV emission, CIII emission and the total radiated power reconstructions are shown in Fig. 3 for attached divertor operation. A similar set of comparisons are shown for detached operation in Fig. 4. In attached operation the profiles

from the lower open divertor [Figs. 3(b,d, f)] show distributed radiation down the outer leg for these high triangularity discharges. In contrast, the profiles from the upper closed divertor. [Figs. 3(a,c,e)] show more localized radiation in the inner leg between the strikepoint and the X–point and in the outer leg near the outer strikepoint. Differences are also seen in detached operation. The lower open divertor shows localized radiation profiles in the outer SOL near the X–point [Figs. 4(b,d,f)]. In contrast, the upper closed divertor during detached outer leg operation shows significant carbon emission (CIV and CIII) down the outer leg near the outer strikepoint region in addition to the emission near the X–point [Figs. 4(a,c,e)]. It should be noted that the profiles from the lower divertor in these high triangularity plasmas with ion ∇B drift into the divertor even show significant differences with previous CIV and CIII profiles in lower triangularity plasmas also with ion ∇B drift into the divertor especially in the attached divertor operation phase [10]. The low triangularity open divertor discharges showed CIV and CIII emission in the inner SOL near the X–point with much less evidence of emission along the length of the outer divertor leg than in these high triangularity discharges.

4. MODELING RESULTS

Divertor simulation results from UEDGE can be compared with data from the tangentially viewing camera systems either as 3-D toroidal image data or as 2-D profiles in a poloidal plane; each has advantages and disadvantages. The basic outputs from the UEDGE simulations are 2-D profiles of emission from the various radiating species in the code calculation plotted on the region that is covered by the UEDGE grid. The basic output from the tangentially viewing cameras is a 3-D image of the emission in the divertor that covers a toroidal angle of about 90 degrees in the tokamak. Tomographic reconstruction techniques [7] can be used to reconstruct 2-D profiles from the 3-D image data assuming toroidal symmetry. However, the reconstruction techniques always introduce some artifacts into the calculated 2-D profiles because of measurement noise in the data and other systematic errors that can not be completely eliminated. On the other hand, a straightforward projection of the UEDGE 2-D solution into a 3-D image that the tangential camera would see, assuming toroidal symmetry, can be done without introducing any artifacts, provided the view of the camera is well known. To compare the basic features of the emission profiles between code and measurement we chose the latter method. Details of the profiles and implications for the plasma physics in the divertor legs of course requires close examination of the 2-D profiles in a poloidal plane.

A comparison of 3-D image data with projections from UEDGE solutions without B-field dependent drifts for the lower divertor at high triangularity [11] shows that UEDGE results match the hydrogenic emission profiles well but do not yet match the CIV profiles in detail. The 3D images of D_α and CIV emission from the lower visible camera are compared with the 3-D projections of the UEDGE solutions for attached and detached conditions in Figs. 5 and 6 respectively. The UEDGE solutions for the attached and detached conditions were obtained by changing the neutral recycling albedo along the walls of the divertor region from 98% to 99% respectively. This difference of a factor of 2 in the effective pumping of neutrals by the divertor walls (from 2% to 1%) produced changes in the D_α profiles that matched the

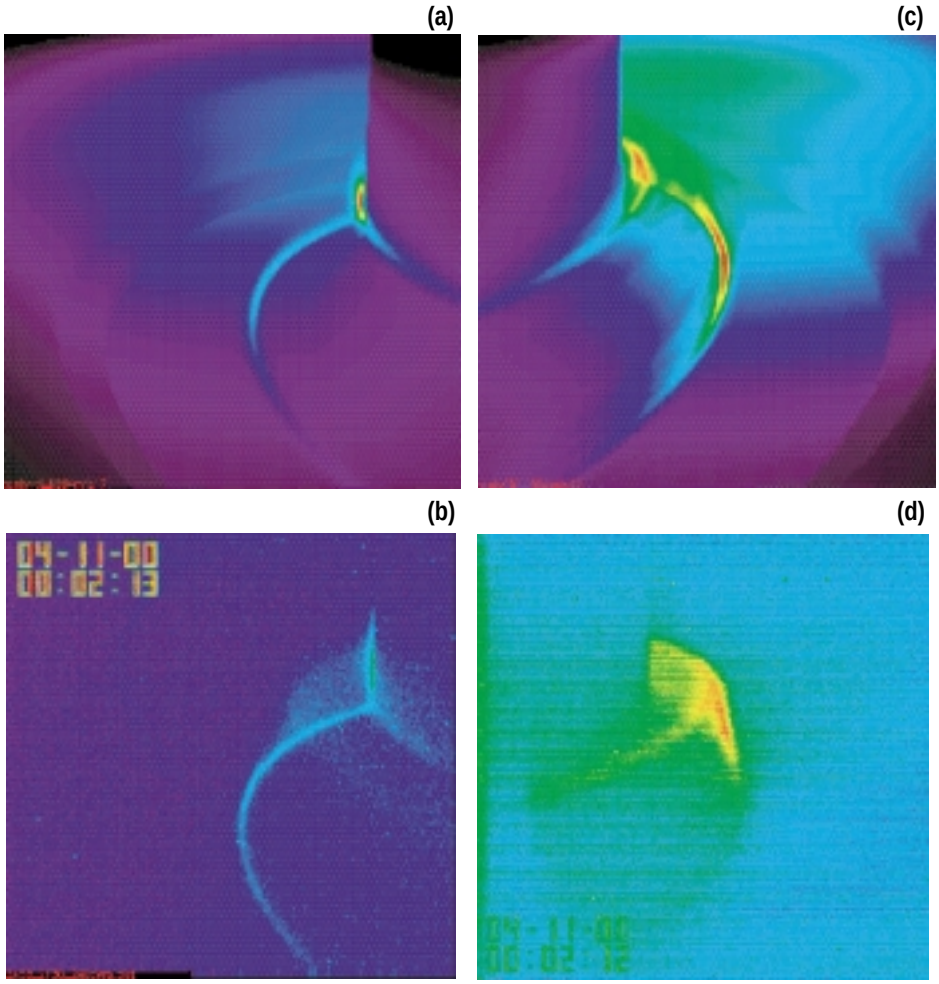

Fig. 5. D_α (a,b) and CIV (c,d) emission profiles (arbitrary units) in 3-D during attached divertor operation of the LSN discharge #102458. UEDGE calculation results are shown in (a,c), data from tangential camera measurements is shown in (b,d). Tokamak centerpost is on the right for (a,b) and on the left for (c,d).

changes seen in the data from attached to detached conditions for this discharge. The 98% recycling solution showed localized D_α emission near both inner and outer separatrix strikepoints [Fig. 5(a)] as seen in the camera image during attached operation [Fig. 5(b)]. The 99% recycling solution showed D_α emission that was more uniformly distributed along the inner and outer divertor legs up to near the X–point [Fig. 6(a)] as seen in the camera data during detached operation [Fig. 6(b)]. The agreement was also very good for $D\gamma$ emission in the two phases of the discharge [11]. However, the comparison of CIV emission in the two phases showed some differences between UEDGE and the data images. In the attached phase [Figs. 5(c),(d)] the UEDGE solution showed local emission zones about half way up both divertor legs between the separatrix strikepoints and the X–point. The camera data was distributed fairly uniformly around the X–point in this case with only limited extension of the emission down the divertor legs. In comparing detached conditions [Figs. 6(c),(d)] the UEDGE simulation showed CIV emission peaked in the inner SOL extending somewhat above the height of the X–point. The camera data showed local CIV emission in the outer SOL that was very local to the height of the X–point.

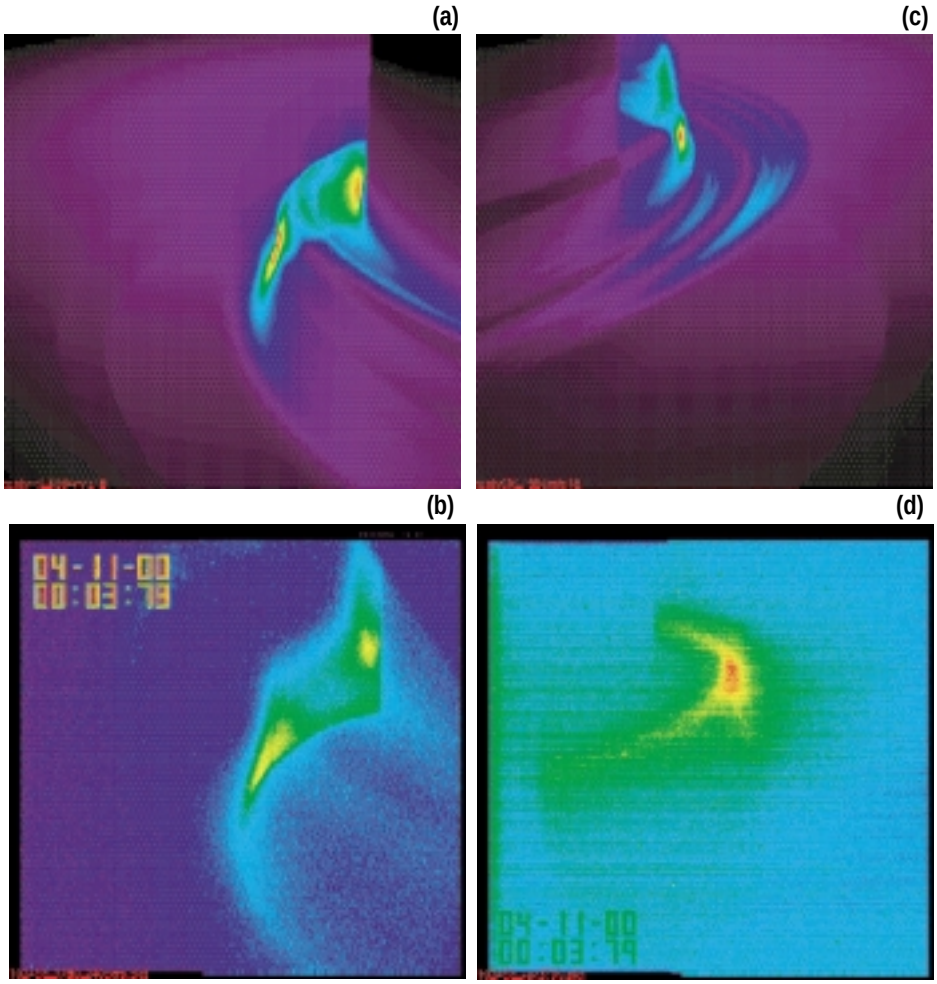

Fig. 6. D_α (a,b) and CIV (c,d) emission profiles (arbitrary units) in 3-D during detached divertor operation of the LSN discharge #102458. UEDGE calculation results are shown in (a,c), data from tangential camera measurements is shown in (b,d). Tokamak centerpost is on the right for (a,b) and on the left for (c,d).

Direct comparison of the 2-D and 3-D profiles from UEDGE and the tangential cameras will help to improve the carbon impurity model in the code and provide further understanding of carbon sources and transport in the divertor. This first attempt to compare UEDGE solutions with VUV CIV at 155 nm in full 2-D profiles shows that some modification of the carbon model is needed that preserves the solution for the total radiated power and the distribution of hydrogenic radiation, which match measurements well now, while changing the profile of the high radiated power CIV emission. In addition, the comparison may indicate that particle drifts that depend on the direction of the magnetic field may play an important role in the 2-D carbon emission profile. Many opportunities exist for advances in the modeling in terms of the location and characteristics of carbon sources, the models of carbon transport and ionization state balance, and modeling of B-field dependent particle drifts.

5. SUMMARY AND CONCLUSIONS

The comparisons presented in this paper show that for high triangularity plasmas there is still the consistency that was seen in previous studies of low triangularity divertor plasmas between the CIV imaging and various other diagnostics measuring radiated power. With

reference to Topic 1, the new data for high triangularity divertor plasma shapes show that CIII radiates in approximately the same regions as CIV as was found in low triangularity plasmas. The CIII visible emission profile is a good indicator of the location of the main carbon radiation (VUV CIV) in both attached and detached divertor operation. Regarding Topic 2, the good qualitative agreement obtained between the carbon radiation profiles and the profiles of total radiated power from reconstructions of bolometer in the low triangularity shapes was also seen in these high triangularity shapes.

The data relevant to Topic 3 show that the geometry of the divertor baffling may make a difference in the radiated power profile from carbon in the divertor although magnetic field dependent particle drifts may also be playing a role in this dataset [13,14]. The differences were more pronounced in attached divertor operation than in detached operation. This would be expected for two reasons. First, when the divertor detaches the ionization/recycling front moves away from the separatrix strikepoints up the divertor legs toward the X–point and the effect of the divertor baffling on the resulting profiles is reduced. Second, the difference in the asymmetries of the divertor plasma induced by the differences in B-field dependent particle drifts between these discharges are expected to be less pronounced when the divertor is detached and the divertor legs are dominated by neutral rather than charged particle transport. This follows from the fact that the strong temperature gradients from the divertor legs to the private flux region, that produce large electric fields in the divertor, are essentially absent in a detached divertor in which the temperature is uniformly low [4]. In the attached cases the CIV emission for low triangularity, open configurations showed a peak in the outer SOL near the X–point. For the high triangularity open divertor with the same ion ∇B drift direction the peak in CIV emission was in an extended region along the outer divertor leg from X–point almost to the target plate. Finally, for the high triangularity baffled case with the opposite ion ∇B drift direction the CIV emission was seen in the inner divertor leg midway between the target plate and the X–point, and also near the outer separatrix strikepoint. It seems clear that divertor plasma geometry (triangularity), baffling structures and B-field dependent drifts can affect the CIV radiation profile.

Finally, UEDGE modeling of the high triangularity open discharge showed very good agreement with measurements of the total radiated power and of the 2-D profile of D_α radiation in the divertor but the detailed 2-D profile of the CIV emission from the simulations shows some differences with the camera measurements. Differences between the code simulations and the CIV measurements could be related to the carbon sources models in the code, the carbon transport model, the fact that the B-field dependent drift models available in the code were not used in these simulations or some combination of these factors. However, since the measurements show appreciable differences in CIV profiles for different divertor geometries there should be ample discrimination in the data to allow validation of future simulations.

ACKNOWLEDGMENT

Work supported by U.S. Department of Energy under Grant DE-FG02-97ER54451, and Contracts W-7405-ENG-48, and DE-AC03-99ER54463.

REFERENCES

[1] ITER Physics Basis Editors, *et al*., Nucl. Fusion **39**, (1999) 2137.

[2] Petrie, T.W., *et al.*, Proc. of the 18th European Conference on Controlled Fusion and Plasma Physics, Berlin, **15C II** (1991) 237, and Petrie, T.W., *et al*., J. Nucl. Mater. **196-198** (1992) 848.

[3] Mahdavi, M.A., *et al.*, Proc. of the 16th IAEA Fusion Energy Conference, Montreal, (1996), IAEA-CN-64/A4-3, I-397.

[4] Fenstermacher M E, Phys. Plasmas (1997) 1761.

[5] Wood, R.D., *et al.*, Proc. 23rd Euro. Conf. On Plasma Phys. And Contr. Fusion, Kiev, Vol. 20C**,** Part II , EPS (1996) p. 763.

[6] Petrie T.W., *et al.*, Nucl. Fusion **37** (1997) 643.

[7] Fenstermacher, M.E., Rev. Sci. Instrum. **68** (1997) 974.

[8] Nilson, D.G., *et al.*, Rev. Sci. Instrum. **70** (1999) 738.

[9] Rognlien, T.D., J. Nucl. Mater. **196-198** (1992) 347.

[10] Fenstermacher, M.E., *et al*., Proc. 26th EPS Conf. On Contr. Fusion and Plasma Physics (Maastricht) Vol. 23J (1999) p. 1197.

[11] Jalufka, N.W., *et al.*, Bull. Am. Phys. Soc. **43** (1998) 1889, Jalufka, N.W., *et al.*, Bull. Am. Phys. Soc. **44**, (1999) 170, avaliable at http://fusion.gat.com/pubs-ext/APS99/ Jalufka_vgs.pdf.

[12] Jalufka, N.W., *et al.*, Bull. Am. Phys. Soc. **45** (2000) 155, available at http://fusion.gat.com/pubs-ext/APS00/Jalufka_pos.pdf.

[13] Chankin, A.V., *et al.*, J. Nucl. Mater. **241-243** (1997) 199, and Chankin, A.V., *et al.*, J. Nucl. Mater. **290-293** (2001) 518.

[14] Petrie, T.W., *et al*., J. Nucl. Mater. **290-293** (2001) 935.